Gamma-ray shielding properties of heavyweight concrete with Electric Arc Furnace slag as aggregate: An experimental and numerical study

Beatrice Pomaro [a], Fabiana Gramegna [b], Roberto Cherubini [b], Viviana De Nadal [b], Valentina Salomoni [c,a,*], Flora Faleschini [a,d]

[a] Department of Civil, Environmental and Architectural Engineering, University of Padova, Via F. Marzolo 9, 35131 Padova, Italy
[b] INFN, National Institute of Nuclear Physics, National Laboratories of Legnaro (PD), Viale dell'Università 2, 35020 Legnaro (PD), Italy
[c] Department of Management and Engineering, University of Padova, Stradella S. Nicola 3, 36100 Vicenza, Italy
[d] Department of Industrial Engineering, University of Padova, Via F. Marzolo 9, 35131 Padova, Italy

HIGHLIGHTS

- Concrete with Electric Arc Furnace steel slag is suitable for radioprotection uses.
- Monte Carlo analyses agree with results from scintillators and dosimetric films.
- EAF concrete has comparable attenuation properties than baritic.
- Baritic concrete has lower mechanical properties than EAF concrete.
- Promising aspects for sustainable heavyweight concrete made with EAF steel slag.

ARTICLE INFO

Keywords:
Electric Arc Furnace slag
Baritic concrete
Heavyweight concrete
Linear attenuation coefficient
Radiation shielding

ABSTRACT

This study investigates, both experimentally and numerically, the radiation shielding properties of two types of heavyweight concretes, one containing barite and one made with Electric Arc Furnace (*EAF*) slag as coarse aggregates. Fresh and hardened concrete properties are preliminary analyzed and compared to a conventional mix containing natural aggregates, namely: fresh and hard bulk density, consistency, compressive and tensile strength, elastic modulus. Three specimens per each mix are subsequently irradiated with both a high-activity (8.97 TBq) and a low-activity (280 kBq) ^{60}Co gamma-ray source to measure their linear attenuation coefficients. Gamma-ray shielding characteristics are also numerically analyzed via a Monte Carlo code assessing radiation transport calculations. Experimental and numerical results indicate that *EAF* concrete has comparable shielding properties to baritic one, and it allows a certain decrease in thickness of the radiation shield, if compared to an ordinary concrete, however it has superior mechanical properties than the other studied mixtures.

1. Introduction

The design of adequate shields is a problem of major concern to guarantee safe service life of existing reactor vessels, nuclear research facilities, as well as strategic structures where accelerators are used for medical and industrial applications. For decades, concrete has been worldwide accepted as an efficient and convenient shielding material. The combined presence of light and heavy nuclei makes it capable to attenuate both neutron and gamma radiations at the same time. Particularly, water content inside concrete has the main role against neutrons, being recommended values for this application in the range 120–170 kg/m^3 in ordinary concretes [1]. Conversely, high-density shields enhance gamma-rays attenuation.

The aggregate choice drives the optimization of concrete radiation shielding properties in a twofold way: i) by adding minerals (e.g. serpentine, limonite) capable of increasing the fixed-water content of concrete or retaining their water of crystallization at high temperatures so to increase the overall water content; and ii) by using heavyweight minerals (typically barite, ferrophosphorus, magnetite, hematite) to increase the specific weight

* Corresponding author at: Department of Management and Engineering, University of Padova, Stradella S. Nicola 3, 36100 Vicenza, Italy.
E-mail addresses: beatrice.pomaro@dicea.unipd.it (B. Pomaro), fabiana.gramegna@lnl.infn.it (F. Gramegna), roberto.cherubini@lnl.infn.it (R. Cherubini), viviana.de.nadal@lnl.infn.it (V. De Nadal), valentina.salomoni@dicea.unipd.it (V. Salomoni), flora.faleschini@dicea.unipd.it (F. Faleschini).

of the mixture. With these additions, it is well-known that enhanced properties can be achieved from the point of view of radioprotection [1–4] and durability [5,6].

Concerning gamma-ray shielding properties, heavyweight concrete is generally expensive. Therefore, several research recently has explored the possibility of using alternative materials, combining good shielding and mechanical properties with cost-effectiveness and sustainability. Lead mine waste aggregates were employed at different replacement ratios in [7], together with barite and limestone; lead slag, both in the form of primary slag and lead-zinc slag waste, was substituted to natural sand in shielding concretes in [8,9]; thermo-chemo-mechanical properties of concrete with fly ash and blast furnace were studied in [10–14]; the influence of pellet waste and trommel sieve waste addition in concrete for shielding purposes was analyzed in [15,16]. The effect of incorporating barite-fluorspar mine waste (BFMW) as a fine aggregate additive on the mechanical and shielding properties of cement mortar has been studied in [17].

In 2016 it was estimated that the total production of steel making slag in Europe was 18.4 million tons, more than 30% of which consisting in Electric Arc Furnace (*EAF*) slag from carbon or stainless/high alloy steel production. The estimated use of the total steel making slag is 14.2 million tons, almost 50% being in road construction and almost 5% in cement and concrete production [18].

EAF slag is a by-product of the iron and steelmaking process in Electric Arc Furnaces. Calcium and iron oxides are the two major chemical constituents of this material, together with SiO_2, Al_2O_3, MnO and MgO. Typically, it has a quite stable crystalline structure, rich in magnetite and hematite [19], which makes it a suitable candidate for gamma-ray radiations shielding applications. However, potential expansive reactions due to the presence of free lime and periclase may hinder a satisfactorily use of this material. They can be prevented by an outdoor weathering of about 2–3 months before use and some daily cycles of drying-wetting conditions [20–22]. A recent work [23] has demonstrated the efficiency of this pre-treatment method (currently adopted by many steelmaking facilities in Italy and Spain for ensuring slag volumetrically stability) and its influence on some physical properties and mineralogical composition. Physical and mechanical properties of *EAF* slag, as well as its chemical composition, can be easily controlled along the steelmaking production chain. Currently, anyway, many producers consider it more a by-product rather than a waste and often its heterogeneity does not differ much from that of a natural material [24].

The characterization of *EAF* slag as coarse recycled aggregate has been addressed by several both in terms of mechanical and durability-related properties of concretes [20,22,25–28]. Some works investigate also the behavior of real scale reinforced concrete (*RC*) elements containing *EAF* slag in whole substitution to coarse natural aggregates (*NAs*), to assess its response at the structural scale, both against gravity load [29,30] and horizontal cyclic loads [31,32]. According to available studies, *EAF* concrete has generally a comparable specific weight to baritic concrete. Mechanical properties are typically enhanced when the slag partially or totally substitutes *NAs*: Pellegrino et al. [20] and Abu-Eishah et al. [33] attributed the observed compressive and tensile strength gain to the slag morphology and shape, which is found to improve the adherence with the cementitious matrix. Faleschini et al. [19] and Arribas et al. [28] observed also that less pores and microcracks are developed in the interfacial transition zone (*ITZ*) of *EAF* concrete than in conventional mixes, thus explaining the typical high strength characterizing *EAF* concrete. Also, the elastic modulus of *EAF* concrete is generally higher than that of a conventional concrete. Hence, the replacement of coarse *NAs* with *EAF* slag allows to design high-strength concretes (*HSC*), maintaining relative high w/c ratios (around 0.4), without using any mineral additions, e.g. high lime fly ashes or silica fume [34].

Recently, some works have attempted preliminary experimental investigations on the radiation shielding properties of *EAF* concretes. Maslehuddin et al. [35] determined that replacing 50% of natural aggregates with *EAF* slag allows to achieve a sustainable and cheap concrete for radiation shielding. González-Ortega et al. [36] compared *EAF* concrete with a conventional and a baritic mixture: from experimental evidences, they obtained that *EAF* concrete was characterized by similar strength to that of ordinary concrete, with intermediate attenuation properties between the other two. Özen et al. [37] demonstrated that concrete with iron ore (hematite), steel slag and natural sand exhibits higher compressive strength and fracture energy than mixes made with steel mill scale, magnetite and barite. These results evidence the capability of such concrete to absorb energy during the cracking process, other than providing an increased linear attenuation coefficient for radiation, which is proportional to the unit weight of the mixture. Ouda [38] compared the shielding properties of several heavyweight concretes made with magnetite, barite, goethite and serpentine as coarse aggregates. Silica fume, fly ash and ground granulated blast furnace slag were also added in the mixes. The optimum solution against gamma-rays was obtained using magnetite both as a coarse and fine aggregate, and an addition of silica fume to the binder. In another study Ouda and Abdel-Gawwad [39] found that the incorporation of basic oxygen furnace (*BOF*) slag at 100% as fine fraction (total replacement of sand) produces a higher packing degree, a reduction in porosity and an improved bulk density, so playing a significant role in gamma-rays attenuation.

In the present work the performance of concrete with 100% *EAF* slag as coarse aggregate is investigated both experimentally and numerically, focusing on the main mechanical parameters and attenuation capacity against gamma-rays. A comparison is conducted in relation to ordinary concrete and another heavyweight mixture: a concrete with 100% barite as coarse aggregate, which is commonly used for radioprotection of nuclear power plants, waste repositories or medical facilities. The combined approach adopted in this work allows proving the soundness of the findings also via a predictive numerical tool, which may be extended to different radiation scenarios or concrete mix proportions.

2. Materials and experimental methods

2.1. Materials and mix details

Three mixtures were investigated, with the aim to assess the influence of aggregate type on the radiation attenuation properties of each concrete: ordinary concrete (*REF*), concrete made with barite (*BAR*) and concrete made with *EAF* slag (*EAF*).

Accordingly, cement dosage and type, w/c ratio and aggregate grading curve were kept constant in all the mixes. For the production of the specimens, a cement type *CEM I 52.5 R* was used at dosage of 400 kg/m^3; w/c ratio was instead 0.4. The use of this type of cement is generally not recommended for massive structures, due to the risks of unfavorable cement hydration temperatures; however, it is here considered for being characterized by low mineral additions, so minimizing possible interaction effects with slag [28].

Concerning the coarse fraction, roundish natural aggregates were used to cast the reference mix; barite was employed to produce the natural heavyweight mix while two sizes of *EAF* slag were used to produce the recycled heavyweight mix. *EAF* slag was obtained from a local plant, where carbon steel is produced; before its use, it was properly pretreated to limit any further expansive reaction. In all the mixes, river sand was used as fine aggregate. Fig. 1 shows the three types of coarse aggregates: a) dolomitic *NA*; b) barite; c) *EAF* slag.

The main physical properties of aggregates are listed in Table 1, and they were evaluated according to EN 933-1:2012 [40] and EN 1097-6:2013 [41], whereas their chemical compositions are reported in Table 2. The coarse aggregates composition differ depending on their origin: natural ones are abundant in calcium and magnesium (alluvial silico-calcareous aggregates); barite aggregates contain minerals consisting of barium sulfate, whereas slag contains high amount of iron, calcium silicon and aluminum, due to their presence in the molten steel bath. Additionally, a water-reducer admixture (*WRA*) was used with the aim of obtaining a S4 consistency class,

Fig. 1. a) Coarse siliceous natural aggregates; b) barite; c) *EAF* slag.

Table 1
Physical characteristics of aggregates.

	NA coarse	Barite	*EAF* slag	*NA* fine
Size (mm)	4–16	4–14	4–16	0–4
Apparent density (kg/m^3)	2701	3817	3854	2703
Water absorption (%)	0.75	1.90	0.84	1.18
Shape	roundish	sharp-pointed	sharp-pointed	roundish

Table 2
Chemical composition of aggregates.

	NA coarse (%)	Barite (%)	*EAF* slag (%)	*NA* fine (%)
CaO	55.74	–	30.30	19.01
SiO_2	4.31	5.01	14.56	53.77
MgO	39.94	–	2.97	10.32
BaO	–	59.86	–	–
SO_3	–	35.14	–	–
Fe_xO_y	–	–	33.28	3.19
Al_2O_3	–	–	10.20	11.90
MnO	–	–	4.34	–
Cr_2O3	–	–	2.67	–
K_2O	–	–	–	1.81

Table 3
Mix proportions of the analyzed concretes (per m^3).

	REF	*BAR*	*EAF*
Cement (kg)	400	400	400
Water (kg)	160	160	160
w/c (–)	0.4	0.4	0.4
NA coarse (kg)	971	–	–
Barite (kg)	–	1371	–
EAF slag (kg)	–	–	1270
NA fine (kg)	913	897	966
Total Volume Aggregates (l)	690	690	690
WRA (kg)	3.2	4.0	3.2

as defined in [42]. Its content varies inside each mixture to achieve the defined workability target. Water was taken from the urban supply system of the city of Padova (Italy), and it does not contain any compound that may affect concrete quality.

The Bolomey grading curve was used to proportion the concretes (Fig. 2). Baritic concrete grading differs more significantly from the other two mixtures because of the difference in the maximum size of the aggregates themselves (barite: d_{max} = 14 mm; *NA* and *EAF*: d_{max} = 16 mm).

Table 3 lists the mix details of the analyzed concretes. It is worth noting that an increase in sand content was necessary in *BAR* and *EAF* mixes to adjust particles grading, due to their different shape with respect to *NAs*.

For each concrete twelve cylindrical specimens ($h \times d$ = 200 × 100 mm^2) and three cubes with 100 mm side were casted. The former were used to assess concrete mechanical properties, i.e. compressive strength at 7 and 28 days, tensile splitting strength and secant elastic modulus at 28 days in agreement with EN 12390 series [43–45]. The latter were instead used to investigate the radiation shielding properties.

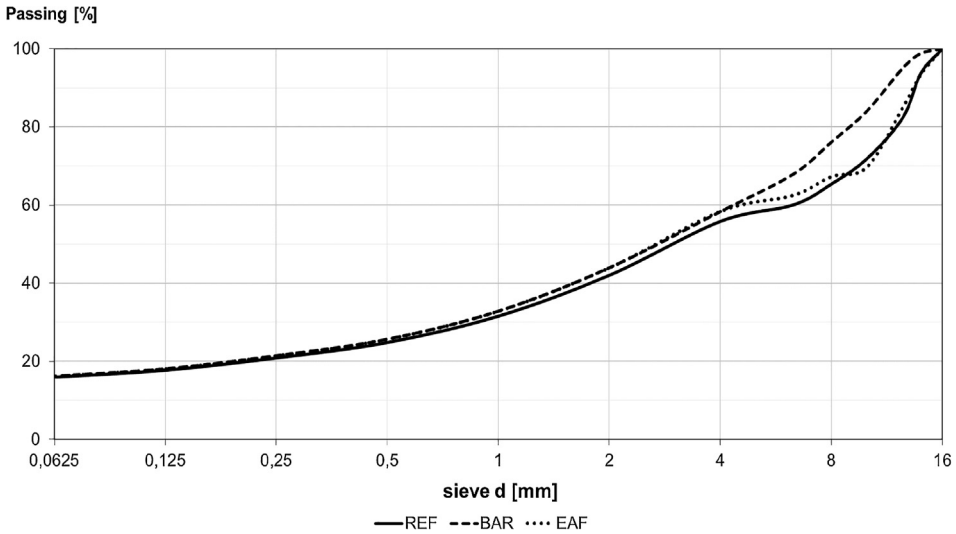

Fig. 2. Particles grading curves (cement + aggregates).

The same mixing and casting procedure was adopted for all specimens to avoid any influence due to possible differences in the preparation conditions. Particularly, samples were properly compacted, demolded after 1 day and then cured in controlled humidity ($RH \geq 95\%$) and temperature conditions (20 ± 1 °C) for 28 days.

2.2. Exposure to gamma-rays and estimation of radiation shielding properties

After the standard 28-days maturation, three cubic specimens per each mix were left in the bunker room hosting the gamma-rays source at the Legnaro National Laboratories (LNL) of the National Institute of Nuclear Physics (INFN) in Legnaro (Padova), Italy, and there exposed for a prolonged period in the perspective of studying also radiation damage on irradiated concrete (which is the object of a future paper). The high-activity ^{60}Co source is of the model Gammabeam 150-A, manufactured by the Atomic Energy of Canada Ltd (Nordion, Canada) [46].

The radioactive source is characterized by an activity of 8.97 TBq (as estimated on July 2016), allowing a dose-rate of 53 Gy/hour at 20 cm from the source; it emits two gamma-rays per decay at average energy of 1.25 MeV.

Fig. 3 shows the location of the specimens around the source, at the chosen radial distance of 20 cm from the source. At this distance, the setup guarantees an isotropic radial irradiation of the samples. This geometrical scenario will be referred from here on as scenario #1.

Part of the incoming radiation I_0 is attenuated by the samples, the remaining part crossing the specimen of thickness x; therefore, the ratio between the intensity detected at the front face (I_0) and that at the back face (I_x) is a measure of the attenuation capacity of the material, through the following expression (Lambert's law) [1]:

$$\mu = \frac{\ln(I_0/I_x)}{x} \tag{1}$$

In Eq. (1) μ is the linear attenuation coefficient, which is defined as the probability per unit distance of travel that a photon of given energy experiences an interaction such as scattering (Compton scattering) or absorption (photoelectric effect and pair production). As the inverse of the mean-free-path λ, the linear attenuation coefficient is also a measure of the average distance that the particle streams from the point where it is generated to the point at which it first interacts with another particle; therefore, it allows an estimate of the material shielding capabilities against photons.

The predominance of the scattering mechanism on the absorption mechanisms varies with the photon energy and the atomic number of the absorber; notably the photoelectric effect is the most sensitive mechanism to the atomic number and it becomes important at low energies. However, the efficiency of both effects increases at increasing atomic number, therefore the attenuation process of photons is driven by the unit weight of a medium.

From the linear attenuation coefficient, the Half-Value Layer (*HVL*) can be calculated, which practically represents the thickness of the absorbing medium required to reduce gamma radiation to one-half of its original intensity. Since the intensity is related to the attenuation coefficient, the *HVL* value can be determined with Eq. (2), which is valid in the case of uncollided mono-energetic photons:

$$HVL = \frac{\ln 2}{\mu} \tag{2}$$

While under broad-beam conditions:

$$\frac{I_x}{I_0} = B\, e^{-\mu x} \tag{3}$$

where B is the buildup factor, which can be obtained by dividing the I/I_0 ratio under broad-beam conditions by the I/I_0 values obtained under narrow-beam conditions. Hence B depends on photon energy, penetration depth and atomic properties of the shield material. Moreover, even the scattering due to the wall of the bunker in which the source is located may contribute to the buildup factor.

A couple of radiochromic films [47] were applied both onto the front and back face of each specimen (with respect to the source exposition), to monitor the irradiation dose uniformity, record the "shielded" dose and then estimate the linear attenuation coefficient of each sample (Fig. 4).

Samples were then exposed to gamma-rays for 6 h; after this period, the pigmentation of the films was analyzed and converted into absorbed dose, via the calibration curve. Analyses of the exposed films, both in the red color channel and multi-channel, were made by using a flat-bed scanner and the NIH ImageJ processing program [48].

An estimate of the linear attenuation coefficient was obtained through Eq. (4), starting from the definition of μ given in Eq. (1), given the direct proportionality between the absorbed dose and the intensity of radiation:

$$\mu = \frac{\ln(D_{in}/D_{out})}{x} \tag{4}$$

where D_{in} and D_{out} are the doses at the front and back face, respectively, and Δx is the thickness of the concrete sample (10 cm).

Radiation attenuation measurements have been performed also using gamma-ray detectors as particle counting instruments. Namely, two types of scintillator have been used: a novel kind of organic scintillators, recently developed at LNL and based on phenyl-polysiloxane (PSS scintillators) [49,50] and an inorganic scintillator made of BaF_2 crystals.

Particularly, organic detectors are proved to overcome the typical drawbacks of both plastic (low radiation hardness and poor stability) and liquid organic detectors (toxicity, flammability, durability) and they show an improved optical transmittance on the scintillation yield as well as thermal and radiation resistance. Their performances, in terms of fluorescence lifetime and neutron/gamma pulse shape discrimination, are discussed in detail in [51]. These detectors are mainly used for neutron detection due to their characteristic low atomic number (they are mainly made by H and C ions) but they can be used even for gammas in high hardness environment for their high resistance and their low efficiency, which may prevent counting build up and saturation of electronics due to high photon fluxes.

Two different geometrical scenarios have been considered for the measurement setups with scintillators: scenario #2 and #3. They both consists in a collimated setup, as schematically pictured out in Fig. 5(a) or in Fig. 5(b), where a low-activity point ^{60}Co source (activity of 280 kBq; dose rate of 6.24×10^{-7} Gy/hour at 40 cm from the source) was used to measure the linear attenuation coefficient. They differ in the point of measurement: in #2 the scintillator is placed in contact

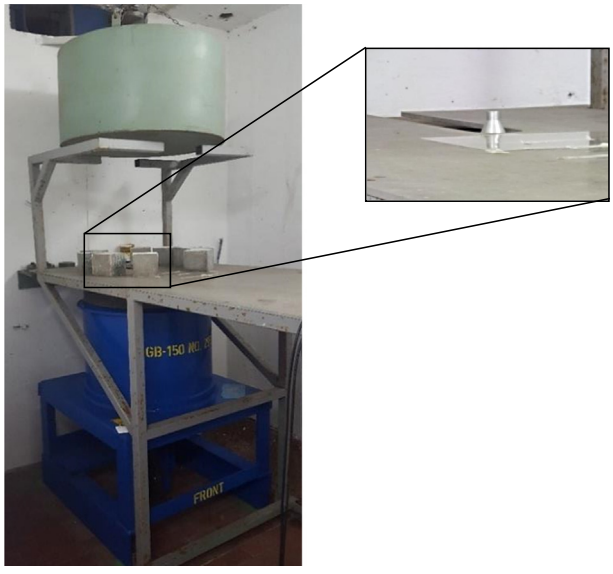

Fig. 3. Test setup for gamma-ray attenuation measurements – detail of the high-activity ^{60}Co source (Gammabeam A150, Nordion, Canada) drawer at rest: experimental scenario #1.

Fig. 4. Radiochromic films applied on the front and back faces of the concrete samples under investigation placed in scenario #1.

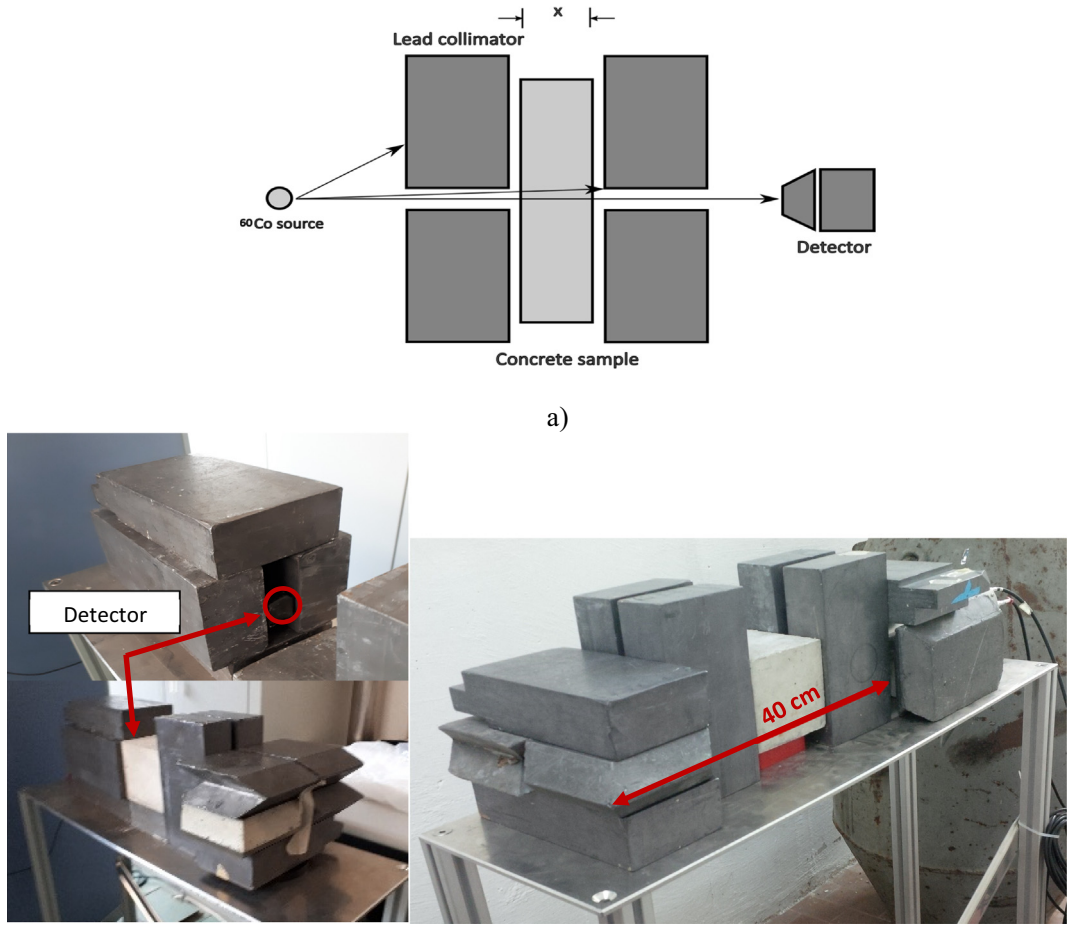

Fig. 5. a) Schematic view of the experimental setup for attenuation coefficient measurement with scintillator detectors; b) picture of the setup: scenario #2 (left): scintillator at 30 cm from the source (i.e. in contact with the concrete samples); scenario #3 (right): scintillator at 40 cm from the source, at further 10 cm lead collimation.

with the back face of the samples; in #3 it is placed at 10 cm from this face, to reduce defects on measurements due to scattering. Measurements were performed using both scintillators: the organic PSS scintillators and the inorganic BaF_2 crystal.

3. Numerical analyses

Photon transport in each irradiated specimen was studied via the Monte Carlo code Fluka® [52,53]. The code was used in the past for studies related to neutron radiation shielding [54,55]; in this work it is employed to specifically address photon transport; in the numerical analyses 10^6 photons were tracked in the analysis to reach an acceptable standard deviation in the simulation; no specific biasing technique was used to improve statistics.

The elemental composition is supposed to be homogeneous for all media (see Table 4). In absence of experimental evidences, a 2% of entrapped air was assumed constant in all the mixtures, based also on the experience that some of the authors developed during a previous experimental campaign for mix design purposes of concretes with *EAF* slag. In the model radiation propagates through dry air.

Fig. 6 shows the photon flux close to the source: front view (a) and top view (b) of the samples. In Fig. 7 results in terms of photon flux for the *REF* sample are reported, for the collimated experimental scenario.

Numerical linear attenuation coefficients were calculated both accounting and neglecting scattering events for a better comparison with experimental results.

4. Results and discussion

4.1. Physical and mechanical properties of fresh and hardened concrete

Table 5 lists the results of fresh and hardened concrete properties. Fresh concrete density, estimated just after casting operations in the molds, was very similar for *BAR* and *EAF* mixtures and higher

Table 4
Elemental composition of the three mixtures implemented in Fluka®; percentage by mass.

	REF (%)	*BAR* (%)	*EAF* (%)
O	37.97	36.01	37.04
Na	0.23	0.20	0.20
Mg	11.77	1.42	2.38
Al	1.87	1.59	4.35
Si	7.76	7.05	9.51
P	0.014	0.002	0.011
S	0.42	7.44	0.36
K	0.44	0.38	0.40
Ca	28.11	8.97	20.01
Mn	0.016	0.007	1.67
Fe	0.81	0.69	12.95
C	9.059	7.70	8.40
N	1.51	1.51	1.51
Ar	0.02	0.02	0.02
H	0.001	0.001	0.001
Cr	–	–	1.21
Ba	–	27.01	–
Density (kg/m^3)	2404	2828	2830

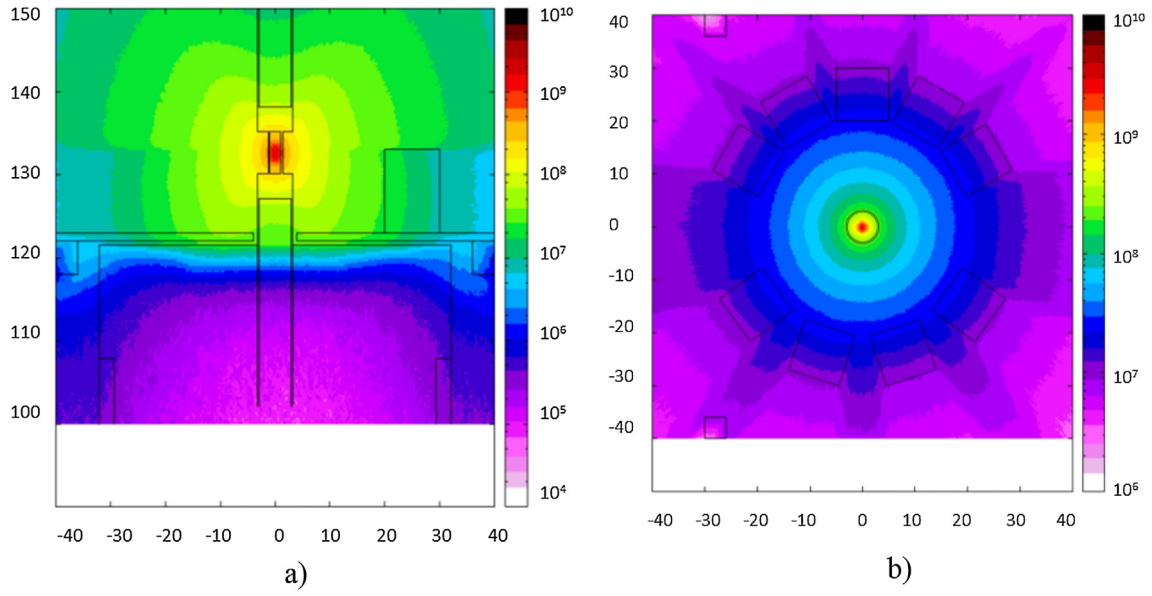

Fig. 6. Photon flux [photons/(cm^2 s)] in the neighborhood of the source: a) front view; b) top view. The simulation refers to the setup of scenario #1.

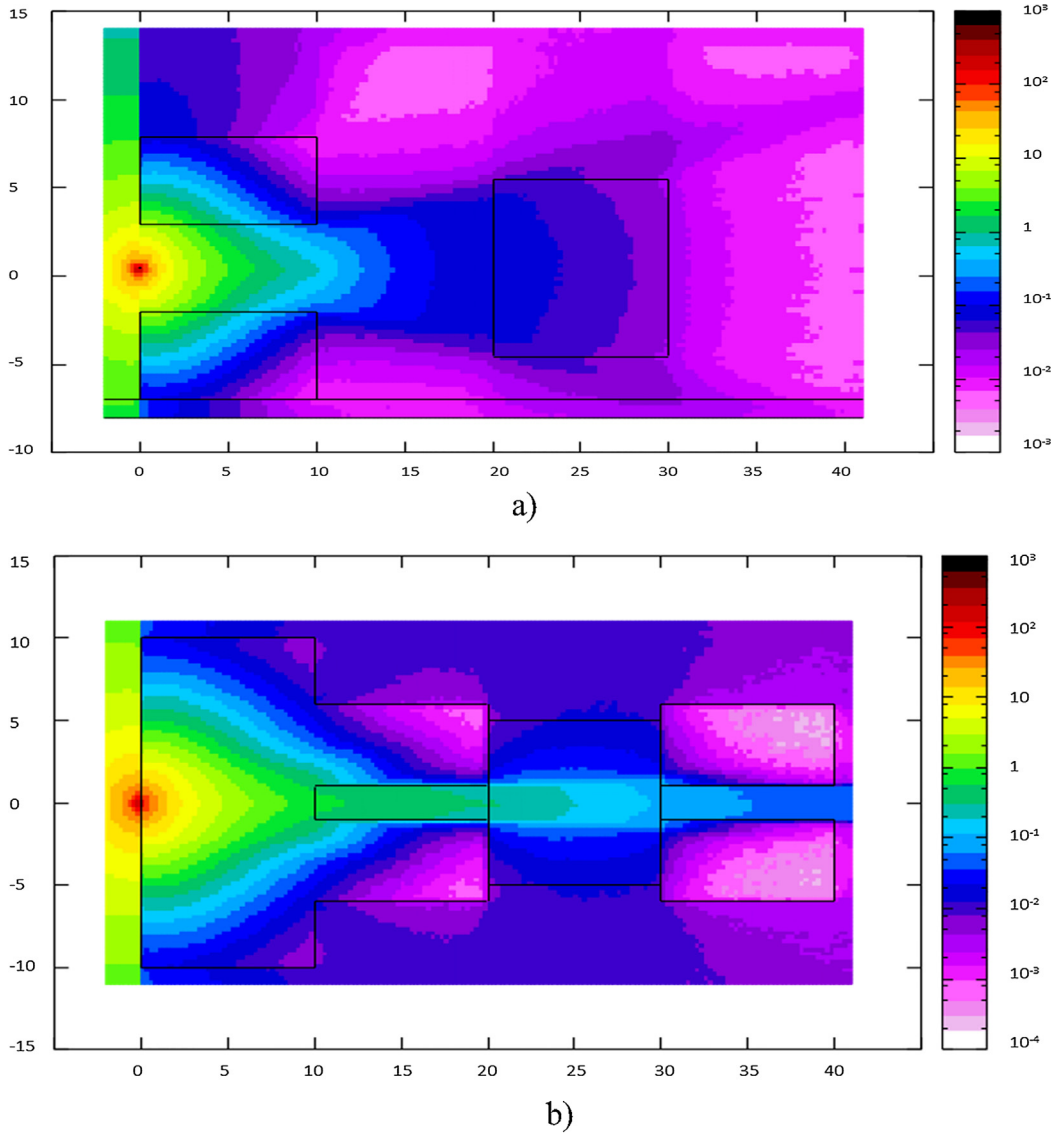

Fig. 7. Photon flux [photons/(cm^2 s)] in the collimated setup with *REF* sample: a) lateral view; b) top view. The simulation refers to scenarios #2 and #3.

than the reference mixture of about +20%. Workability, assessed with the Abrams cone method, is in the range of quasi-fluid and fluid classes. Particularly, one can appreciate that the slight addition of *WRA* and fine particles in the *EAF* mixture was effective in improving the workability of fresh concrete. This did not occur in the case of *BAR*, in which the mix design variation involved only the amount of fine particles, whereas the *WRA* content was kept constant as in the reference batch. This explains why *BAR* showed a lower slump than the other two mixtures.

When considering concrete strength evolution, *EAF* mixture displays higher compressive strength from the first days of maturation, with an increase of the 7-days compressive strength of +27% and +28% if compared to *REF* and *BAR* mixtures, respectively. These latter are instead characterized by a similar strength at early age. At 28 days the difference in compressive strength further increases up to +29% and +32%, respectively. Such results are consistent with the literature on the positive effects of using *EAF* slag in hydraulic mixes [19,23–28].

Tensile strength increases considerably in *EAF* concrete if compared to *REF* and *BAR* mixes, with an improvement of about +22% in both cases.

The splitting surfaces of the tested samples are shown in Fig. 8.

Elastic properties, evaluated in terms of the secant elastic modulus, are found to be enhanced when *EAF* slag is used as coarse aggregate: in this case the improvement is of +25% if compared to the *REF* mix, and even +41% if compared to *BAR*. This result indicates that baritic aggregates are made by softer, more fragile minerals than *EAF* slag, even though the specific weight of the two is comparable. Indeed, negligible differences in density are observed in hardened *BAR* and *EAF* at 28 days of curing.

4.2. Radiation shielding properties

Fig. 9 shows the average linear attenuation coefficient of the three analyzed mixtures, numerically computed via Fluka® code with scenario #1 for the experimental setup; the numerical results correspond to the three filled black symbols in the same figure, which are an average of the values obtained for the three samples per mix of the simulation. Results are here compared with the experimental data obtained from an extensive campaign on various concrete mixes reported in [56]. The plot shows how the attenuation capability of concrete is strongly linearly proportional to its density, as experimentally assessed in [56]. The results obtained from the numerical simulations are found to closely match the available data with an error of ±1.63% on the fluxes. Particularly, the *REF* mix is fairly in line with the shielding performance of ordinary concretes of medium-to-high density, while both *BAR* and *EAF* mixtures show a shielding capacity close to that proper of a baritic concrete of medium density; the attenuation coefficient of the two is very similar, due to the similar unit weight of the mixtures themselves.

The comparison between numerical and experimental results obtained for the different approaches and the different studied sce-

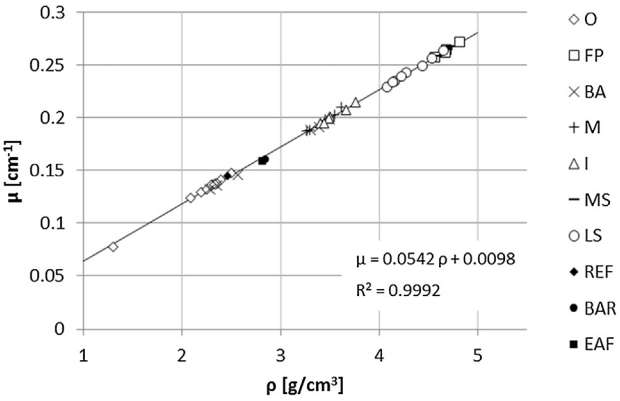

Fig. 9. Numerical results for the linear attenuation coefficient of the tested mixtures, obtained by numerical simulation of scenario #3: ordinary concrete (*REF*), baritic concrete (*BAR*) and concrete enriched with *EAF* slag (*EAF*), compared to experimental values of several concretes exposed to photons of 1.25 MeV energy (*O*-ordinary concrete; *FP*-ferrophosphorus concrete; *BA*-baritic concrete; *M*-magnetite concrete; I-ilmenite concrete; *MS*-magnetite-steel concrete) (Experimental data redrawn from [56]).

Table 5
Fresh and hardened properties of the investigated concretes.

	Fresh density (kg/m^3)	Slump (cm)	$f_{c\ 7days}$ (MPa)	Dry density $_{28\ days}$ (kg/m^3)	$f_{c\ 28days}$ (MPa)	f_{ct} (MPa)	E_c (MPa)
REF	2379	–	35.5	2396	41.49	2.64	36,686
	2399	–	34.4	2409	41.07	3.52	35,297
	2392	–	30.8	2407	41.16	3.81	37,066
Average	2390	19	33.5	2404	41.24	3.32	36,350
BAR	2853	–	29.2	2794	40.59	3.25	28,783
	2874	–	34.6	2843	39.88	3.16	28,115
	2926	–	35.6	2847	38.72	3.67	29,115
Average	2884	15	33.2	2828	39.7	3.36	28,671
EAF	2813	–	47.0	2805	59.2	3.97	46,538
	2800	–	45.7	2820	55.5	4.44	49,609
	2837	–	45.3	2869	59.3	4.31	49,869
Average	2817	21	46.0	2830	58.0	4.24	48,672

Fig. 8. Splitting surfaces of the tested concretes: a) *REF*; b) *BAR*; c) *EAF* mixtures.

narios are reported in Table 6, in terms of linear attenuation coefficients μ and half-value layer *HVL*.

The attenuation coefficients determined via the use of the dosimetric films have been obtained through Eq. (4) (Section 2.2) with D_{in} and D_{out} corresponding to the dose without (i.e., "in air") and with the concrete sample placed in front of the film, respectively, for each one of the three samples of each studied mix, in such a way that all geometrical and intrinsic efficiencies could be cancelled in the ratio and, therefore, neglected. In the same way, the attenuation coefficients determined via the use of scintillators have been obtained through Eq. (1) with I_0 and I_x corresponding to the gamma-ray particles counted without and with the concrete sample placed in between the source and the detector, respectively; similarly, the numerically obtained attenuation coefficients still come from Eq. (1) in which I_0 and I_x correspond now to the gamma-ray fluxes computed at a same distance × without and with the sample. The half-value layer has been computed, in any case, through Eq. (2).

μ and *HVL* for each mix type come from averaging the three values obtained per each sample. The experimental errors in Table 6 refer to standard deviations.

Numerical results are associated to an average error on the fluxes of ±0.65% for scenario #1 and ±1.63% for scenarios #2 and #3.

By comparing the results of Table 6(a), it can be noticed that the results obtained via the dosimetric films (scenario #1) appear in general much higher (in terms of linear attenuation coefficient) than those measured via the scintillators and the numerical ones,

Table 6
Comparison of experimental and numerical results: the linear attenuation coefficient μ (upper table) and the Half Value Layer (*HVL*) (lower table): a) scenario #1: dosimetric films b) scenario #2: scintillator at 30 cm from the source (i.e. in contact with the concrete samples) using a low-activity point ^{60}Co gamma-ray source. c) scenario #3: scintillator at 40 cm from the source using a low-activity point ^{60}Co gamma-ray source. d) scenario #2 (left): scintillator at 30 cm from the source (i.e. in contact with the concrete samples) and scenario #3 (right): scintillator at 40 cm from the source, both using a low-activity point ^{137}Cs gamma-ray source.

(a)

μ [cm^{-1}]

	Experimental dosimetric film (scenario #1)	Numerical (scenario #1)	Numerical (scenario #1) No scattering
REF	0.163 ± 0.003	0.068	0.115
BAR	0.181 ± 0.003	0.078	0.128
EAF	0.182 ± 0.001	0.090	0.126

HVL [cm]

	Experimental dosimetric film (scenario #1)	Numerical (scenario #1)	Numerical (scenario #1) No scattering
REF	4.257 ± 0.08	10.168	6.010
BAR	3.841 ± 0.07	8.901	5.420
EAF	3.804 ± 0.02	7.682	5.494

(b)

μ [cm^{-1}]

	Experimental PSS (scenario #2)	Experimental BaF_2 (scenario #2)	Numerical (scenario #2)	Numerical (scenario #2) No scattering
REF	0.095 ± 0.002	0.106 ± 0.002	0.082	0.144
BAR	0.112 ± 0.002	0.121 ± 0.002	0.098	0.160
EAF	0.111 ± 0.002	0.120 ± 0.002	0.095	0.159

HVL [cm]

	Experimental PSS (scenario #2)	Experimental BaF_2 (scenario #2)	Numerical (scenario #2)	Numerical (scenario #2) No scattering
REF	7.275 ± 0.160	6.510 ± 0.125	8.409	4.829
BAR	6.211 ± 0.124	5.705 ± 0.104	7.039	4.325
EAF	6.219 ± 0.125	5.784 ± 0.105	7.308	4.354

(c)

μ [cm^{-1}]

	Experimental PSS (scenario #3)	Experimental BaF_2 (scenario #3)	Numerical (scenario #3)	Numerical (scenario #3) No scattering
REF	0.130 ± 0.004	0.121 ± 0.004	0.124	0.145
BAR	0.148 ± 0.004	0.139 ± 0.004	0.138	0.160
EAF	0.150 ± 0.005	0.152 ± 0.005	0.141	0.158

HVL [cm]

	Experimental PSS (scenario #3)	Experimental BaF_2 (scenario #3)	Numerical (scenario #3)	Numerical (scenario #3) No scattering
REF	5.341 ± 0.165	5.704 ± 0.176	5.574	4.779
BAR	4.660 ± 0.140	4.969 ± 0.152	5.024	4.333
EAF	4.617 ± 0.139	4.554 ± 0.138	4.931	4.385

(d)

μ [cm^{-1}]

	Experimental PSS (scenario #2) – ^{137}Cs	Experimental BaF_2 (scenario #2) – ^{137}Cs	Experimental PSS (scenario #3) – ^{137}Cs	Experimental BaF_2 (scenario #3) – ^{137}Cs
REF	0.140 ± 0.003	0.147 ± 0.003	0.169 ± 0.006	0.162 ± 0.010
BAR	0.167 ± 0.003	0.173 ± 0.003	0.200 ± 0.007	0.181 ± 0.012
EAF	0.162 ± 0.003	0.175 ± 0.003	0.199 ± 0.008	0.179 ± 0.013

HVL [cm]

	Experimental PSS (scenario #2) – ^{137}Cs	Experimental BaF_2 (scenario #2) – ^{137}Cs	Experimental PSS (scenario #3) – ^{137}Cs	Experimental BaF_2 (scenario #3) – ^{137}Cs
REF	4.951 ± 0.107	4.707 ± 0.087	4.112 ± 0.150	4.291 ± 0.278
BAR	4.159 ± 0.083	4.016 ± 0.078	3.462 ± 0.130	3.827 ± 0.230
EAF	4.287 ± 0.089	3.968 ± 0.076	3.489 ± 0.133	3.864 ± 0.249

when the build-up effect is accounted for. On the other hand, they are closer to the numerical predictions when the scattering effects are not taken into account. The observed differences may be due to the fact that, since dosimetric films are much thinner than scintillators and mounted directly on the specimen back face, as described in Section 2.2, they may be poorly influenced by scattering events unless scattered gammas are almost perpendicular to their sensitive face.

In any case, both experimental and numerical results confirm the better and comparable shielding features of *BAR* and *EAF* with respect to *REF*.

As for the measurements with scintillators, the collimated measurement setup sketched in Fig. 5 is proved to better control the drawback derived by the open geometry of the experiment: scenario #2, where the detector is in contact with the concrete sample, shows that still strong scattering effects may influence the results (up to 1.8–1.9 more gamma-rays than expected, behind the sample), but they are well accounted for by the numerical results, which are practically the same in scenarios #2 and #3, when the build-up factor is washed out. In scenario #3 the overall effect of scattering is very much reduced (<20%). Moreover, the numerical values obtained in scenario #3, corrected for the scattering effects, are also very close to the numerical results obtained by considering an optimum geometry with an infinitely wide concrete wall and a perfectly collimated beam (μ equal to 0.142, 0.159 and 0.161 cm^{-1} respectively for *REF*, *BAR* and *EAF* mixtures).

By comparing the three samples, the experimental results show that the *EAF* mix is similar or even slightly more performant than the *BAR* one, and they both are better than the *REF* mix in terms of gamma-rays attenuation capacity. This seems to be more evident in the measurements performed with the BaF_2 scintillator, which is sensitive also to the photoelectric phenomenon, not only to Compton scattering (as is the case of the organic scintillator).

A similar behavior between baritic concrete and concrete made with *EAF* slag aggregates has been numerically confirmed, and almost no differences are envisaged when correcting for the build-up effects. On the other side, standard concrete exhibits lower shielding capacities, both experimentally and numerically.

In terms of *HVL*, for a given radiation field, the performance of heavyweight concretes can be appreciated if compared to ordinary concrete. By considering the results from scenario #1, *EAF* slag and baritic concretes are proved to allow for a decrease in the shielding thickness (to attenuate the same amount of incident photons) of 18 and 19%, respectively, with respect to an ordinary concrete when considering the results from scintillators (which are inclusive of scattering effects); these percentages are almost confirmed by the numerical calculations conducted in the same configuration. When comparing the results obtained via the dosimetric films and the calculations corrected for the scattering effects, a more realistic decrease of 10 and 11% is obtained, respectively. A similar outcome is found from the experimental values in scenario #3, leading to a decrease in the shielding thickness at the scintillator position (plastic detector) of 13 and 14%, respectively, and a decrease of 13 and 20% for the BaF_2 scintillator.

These results are confirmed by the numerical values, which give a thickness decrease of approximately 10% for the two heavyweight mixtures, both when scattering occurs and when build-up is avoided.

A further confirmation of these results, in terms of a major screening of the *EAF* mix with respect to ordinary concrete but comparable with the *BAR* mix, comes from Table 6(d), which reports the data taken in scenarios #2 and #3, by using a ^{137}Cs point gamma-ray source, characterized by an activity of 280 kBq and a lower energy gamma emission $E_\gamma = 0.6617$ MeV.

The reduced *HVL* ($\sim$20%) found with respect to the same measures obtained with the ^{60}Co source, i.e. the concrete thickness needed to screen the softer ^{137}Cs gamma-rays, is in agreement with what reported in literature.

A comparison of the results obtained in broad-beam irradiation conditions with respect to those in a perfectly collimated condition allows also to numerically quantify the buildup factor *B* as 1.31 for *REF*, 1.36 for *BAR* and 1.42 for *EAF* mixture. Minor differences are encountered in terms of experimental evidences; in this case: 1.23 for *REF*, 1.25 for *BAR* and 1.23 for *EAF* mixture, which might indicate a major effect of the common collimation material with respect to the contents of the different specimens.

5. Conclusions

The feasibility of using *EAF* slag as a heavyweight aggregate to produce concrete for structural as well as radiological shielding purposes has been here discussed and proved.

Two experimental equipments have been used to evaluate attenuation capabilities against gamma-rays of concrete made with *EAF* steel slag as coarse aggregate: radiochromic dosimetry films and scintillator detectors. The experimental setup has been reconstructed via the Monte Carlo code Fluka® both in a non-collimated and collimated testing geometry. The study of different scenarios have allowed for confirming that several phenomena (among which photons scattering and lead shielding effects) can affect the measurements, so suggesting deep care when interpreting the results.

Since the shielding capability against gamma-rays is highly affected by the density of the medium, for concrete it may be conveniently controlled by the choice of aggregates, which are the larger constituent of the mix design. *EAF* slag exhibits densities that are in line with heavyweight concretes used for radioprotection issues, like baritic concretes. At the same time its mechanical performance is higher than that of ordinary as well as of baritic concretes (whose drawback is the fragile nature of barite aggregates), in terms of compressive, tensile strength and elastic modulus.

Concrete with *EAF* slag has a compressive strength +29% and +32% greater than that of ordinary and baritic concrete, respectively, turning to +25% and +41% if the elastic modulus is considered.

The shielding properties of concretes with *EAF* slag are similar or even higher than the measured or calculated ones for baritic concrete and, in all cases, they are significantly enhanced if compared to ordinary concrete. In addition, the required thickness to halve the initial intensity of photons is relatively similar for baritic concrete and concrete made with *EAF*.

Particularly, for a given radiation intensity, numerical and experimental evidences have demonstrated that an ordinary concrete wall needs to be about 10–20% thicker than one made with 100% *EAF* slag aggregates to obtain the same shielding capacity.

Correspondingly, the Electric Arc Furnace oxidizing slag has here appeared to be a promising by-product for its sustainable use in concrete production even in the field of radiological protection.

Conflict of interest

None.

Acknowledgments

Financial support from the University of Padua, Italy, in the framework of BIRD 2016 Project – BIRD163134/16 and PRAT 2015 Project – CPDA151808, is gratefully acknowledged.

The authors would like to thank Dr. Anna Berno for her contribution during her Master Degree Thesis and Dr. Daniela Fabris for her help during the experimental campaign. Zerocento S.r.l., Italcementi-Heidelberg S.p.A. and SVA S.r.l. are acknowledged for supplying respectively *EAF* slag, cement and baritic aggregates.

References

[1] R.G. Jaeger, Engineering Compendium On Radiation Shielding, Springer, Berlin, 1970.
[2] B.T. Price, C.C. Horton, K.T. Spinney, Radiation Shielding, Pergamon Press, London, 1957.
[3] A.N. Komarovskii, Shielding Materials for Nuclear Reactors, Pergamon Press, London, 1961.
[4] M.F. Kaplan, Concrete radiation shielding: nuclear physics, concrete properties, design, and construction, John Wiley & Sons, New York, 1989.
[5] B. Pomaro, V.A. Salomoni, F. Gramegna, G. Prete, C.E. Majorana, Radiation damage evaluation on concrete within a facility for Selective Production of Exotic Species (SPES Project), Italy, J. Hazard. Mater. 194 (2011) 169–177.
[6] B. Pomaro, A review on radiation damage in concrete for nuclear facilities: from experiments to modeling, Modell. Simul. Eng. 2016 (2016).
[7] M. Çullu, H. Ertaş, Determination of the effect of lead mine waste aggregate on some concrete properties and radiation shielding, Constr. Build. Mater. 125 (2016) 625–631.
[8] M. Alwaeli, Investigation of gamma radiation shielding and compressive strength properties of concrete containing scale and granulated lead-zinc slag wastes, J. Clean. Prod. 166 (2017) 157–162.
[9] N. Saca, L. Radu, V. Fugaru, M. Gheorghe, I. Petre, Composite materials with primary lead slag content: application in gamma radiation shielding and waste encapsulation fields, J. Clean. Prod. 179 (2018) 255–265.
[10] R. Demirboğa, İ. Turkmen, M.B. Karakoç, Relationship between ultrasonic velocity and compressive strength for high-volume mineral-admixtured concrete, Cem. Concr. Res. 34 (12) (2004) 2329–2336.
[11] R. Demirboğa, İ. Turkmen, M.B. Karakoç, Thermo-mechanical properties of concrete containing high-volume mineral admixtures, Build. Environ. 42 (1) (2007) 349–354.
[12] İ. Turkmen, R. Gul, C. Celik, A Taguchi approach for investigation of some physical properties of concrete produced from mineral admixtures, Build. Environ. 43 (2008) 1127–1137.
[13] K. Singh, S. Singh, A.S. Dhaliwal, G. Singh, Gamma radiation shielding analysis of lead-fly ash concretes, Appl. Radiat Isot 95 (2015) 174–179.
[14] O. Gencel, F. Koksal, C. Ozel, W. Brostow, Combined effect of fly ash and waste ferrochromium on properties of concrete, Constr. Build. Mater. 29 (2012) 633–640.
[15] R. Boncukcuoğlu, O. İcelli, S. Erzeneoğlu, Kocakerim M. Muhtar, Comparison of radioactive transmission and mechanical properties of Portland cement and modified cement with trommel sieve waste, Cem. Concr. Res. 35 (2005) 1082–1087.
[16] O. Icelli, Z. Yalcin, M. Okutan, R. Boncukcuoğlu, Determination of photon energy absorption parameters for pellet waste, trommel sieve waste and original tincalconite, Ann. Nucl. Energy 47 (2012) 38–45.
[17] W. Gallala, Y. Hayouni, M.E. Gaied, M. Fusco, J. Alsaied, K. Bailey, M. Bourham, Mechanical and radiation shielding properties of mortars with additive fine aggregate mine waste, Ann. Nucl. Energy 101 (2017) 600–606.
[18] Euroslag (http://www.euroslag.com/products/statistics/2016/)
[19] F. Faleschini, K. Brunelli, M.A. Zanini, M. Dabalà, C. Pellegrino, Electric Arc furnace as coarse recycled aggregate for concrete production, J. Sustain. Metall. 2 (1) (2016) 44–50.
[20] C. Pellegrino, P. Cavagnis, F. Faleschini, K. Brunelli, Properties of concretes with black/oxidizing electric arc furnace slag aggregate, Cem. Concr. Comp. 37 (2013) 232–240.
[21] M.N.-T. Lam, S. Jaritngam, D.-H. Le, Roller-compacted concrete pavement made of electric Arc Furnace slag aggregate: mix design and mechanical properties, Constr. Build. Mater. 154 (2017) 482–495.
[22] J.M. Manso, J.A. Polanco, M. Losañez, J.J. González, Durability of concrete made with EAF slag as aggregate, Cem. Concr. Comp. 28 (2006) 528–534.
[23] A. Santamaria, F. Faleschini, G. Giacomello, K. Brunelli, J.-T. San-Josè, C. Pellegrino, M. Pasetto, Dimensional stability of Electric Arc furnace slag in civil engineering applications, J. Clean. Prod. 205 (2018) 599–609.
[24] C. Pellegrino, F. Faleschini, Electric arc furnace slag concrete, Sustainability Improvements in the Concrete Industry", Green Energy and Technology, Springer, 2016.
[25] M. Maslehuddin, A.M. Sharif, M. Shameem, M. Ibrahim, M.S. Barry, Comparison of properties of steel slag and crushed limestone aggregate concretes, Constr. Build. Mater. 17 (2003) 105–112.
[26] F. Faleschini, A. Santamaria, M.A. Zanini, J.T. San José, C. Pellegrino, Bond between steel reinforcement bars and electric arc furnace slag concrete, Mater. Struct. 50 (3) (2017).
[27] I. Papayianni, E. Anastasiou, Production of high-strength concrete using high volume of industrial by-products, Constr. Build. Mater. 24 (2010) 1412–1417.
[28] I. Arribas, A. Santamaría, E. Ruiz, V. Ortega-López, J.M. Manso, Electric arc furnace slag and its use in hydraulic concrete, Constr. Build. Mater. 90 (2015) 68–79.
[29] C. Pellegrino, F. Faleschini, Experimental behavior of reinforced concrete beams with electric arc furnace slag aggregate, ACI Mater. J. 110 (2) (2013) 197–205.
[30] A.W. Kim, Y.S. Kim, J.M. Lee, K.H. Kim, Structural performance of spirally confined concrete with EAF oxidizing slag aggregate, Eur. J. Environ. Civ. Eng. 17 (8) (2013) 654–674.
[31] F. Faleschini, L. Hofer, M.A. Zanini, M. dalla Benetta, C. Pellegrino, Experimental behavior of beam-column joints made with EAF concrete under cyclic loading, Eng. Struct. 139 (2017) 81–95.
[32] J.-M. Lee, Y.-J. Lee, Y.-J. Jung, J.-H. Park, B.-S. Lee, K.-H. Kim, Ductile capacity of reinforced concrete columns with electric arc furnace oxidizing slag aggregate, Constr. Build. Mater. 162 (2018) 781–793.
[33] S.I. Abu-Eishah, A.S. El-Dieb, M.S. Bedir, Performance of concrete mixtures made with electric arc furnace (EAF) steel slag aggregate produced in the Arabian Gulf region, Constr. Build. Mater. 34 (2012) 249–256.
[34] F. Faleschini, M.A. Fernández-Ruíz, M.A. Zanini, K. Brunelli, C. Pellegrino, E. Hernández-Montes, High performance concrete with electric arc furnace slag as aggregate: mechanical and durability properties, Constr. Build. Mater. 101 (2015) 113–121.
[35] M. Maslehuddin, A.A. Naqvi, M. Ibrahim, Z. Kalakada, Radiation shielding properties of concrete with electric arc furnace slag aggregates and steel shots, Ann. Nucl. Energy 53 (2013) 192–196.
[36] M.A. González-Ortega, I. Segura, S.H.P. Cavalaro, B. Toralles-Carbonari, A. Aguado, A.C. Andrello, Radiological protection and mechanical properties of concretes with EAF steel slags, Constr. Build. Mater. 51 (2014) 432–438.
[37] S. Özen, C. Şengül, T. Erenoğlu, Ü. Çolak, İ.A. Reyhancan, M.A. Taşdemir, Properties of heavyweight concrete for structural and radiation shielding purposes, Arab J. Sci. Eng. 41 (4) (2016) 1573–1584.
[38] A.S. Ouda, Development of high-performance heavy density concrete using different aggregates for gamma-ray shielding, Prog. Nucl. Energy 79 (2015) 48–55.
[39] A.S. Ouda, H.A. Abdel-Gawwad, The effect of replacing sand by iron slag on physical, mechanical and radiological properties of cement mortar, HBRC J. 13 (3) (2017) 255–261.
[40] EN 933-1:2012. Tests for geometrical properties of aggregates – Part 1: Determination of particle size distribution – Sieving method.
[41] EN 1097-6:2013. Tests for mechanical and physical properties of aggregates – Part 6: Determination of particle density and water absorption.
[42] EN 206-1, Concrete – Part 1: Specification, Performance, Production and Conformity, Comité Europeen de Normalisation, Brussels, Belgium, 2006.
[43] EN, 12390–4, Testing Hardened Concrete – Compressive Strength – Specification for Testing Machines, Comité Européen de Normalisation 2000 Brussels, Belgium
[44] EN 12390-6, Testing Hardened Concrete – Tensile Splitting Strength of Test Specimens, Comité Européen de Normalisation, Brussels, Belgium, 2009.
[45] EN, 12390–13, Testing Hardened Concrete – Part 13: Determination of Secant Modulus of Elasticity in Compression, Comité Européen de Normalisation 2013 Brussels, Belgium
[46] AEC/Nordion (gamma source) handbook; Nordion (Canada) Inc (http://www.nordion.com/gamma-technologies/).
[47] Gafchromic film datasheet (http://www.gafchromic.com/documents/gafchromic-hdv2.pdf).
[48] ImageJ software (http://imagej.net/index.html).
[49] S. Carturan, A. Quaranta, T. Marchi, F. Gramegna, M. Degerlier, M. Cinausero, V. L. Kravchuk, M. Poggi, Novel polysiloxane-based scintillators for neutron detection, Radiat. Prot. Dosim 143 (2–4) (2011) 471–476.
[50] M. Degerlier, S. Carturan, F. Gramegna, T. Marchi, Palma M. Dalla, M. Cinausero, G. Maggioni, A. Quaranta, G. Collazuol, J. Bermudez, Novel scintillating materials based on phenyl-polysiloxane for neutron detection and donitoring, in: E. Polychroniadis, A. Oral, M. Ozer (Eds.), International Multidisciplinary Microscopy Congress. Springer Proceedings in Physics, Springer, Cham, 2014.
[51] Palma M. Dalla, T. Marchi, S. Carturan, C. Checchia, G. Collazuol, F. Gramegna, N. Daldosso, V. Paterlini, A. Quaranta, M. Cinausero, M. Degerlier, Pulse shape discrimination in polysiloxane-based liquid scintillator, IEEE Trans. Nucl. Sci. 63 (3) (2016) 1608–1615.
[52] A. Ferrari, P. R. Sala, A. Fassò, J. Ranft, "FLUKA: a multi-particletransport code". CERN-2005-10, INFN/TC_05/11, SLAC-R-773, 2005.
[53] T.T. Böhlen, F. Cerutti, M.P.W. Chin, A. Fassò, A. Ferrari, P.G. Ortega, A. Mairani, P.R. Sala, G. Smirnov, V. Vlachoudis, The FLUKA code: developments and challenges for high energy and medical applications, T.T Nuclear Data Sheets 120 (2014) 211–214.
[54] B. Pomaro, V.A. Salomoni, F. Gramegna, G. Prete, C.E. Majorana, Radiation damage evaluation on concrete shielding for nuclear physics experiments, Ann. Solid Struct. Mech. 2 (2011) 123–142.
[55] C.E. Majorana, V.A. Salomoni, B. Pomaro, G. Xotta, F. Gramegna, Macro- and meso-scale analysis of concrete as a multiphase material for biological shields against nuclear radiation, Int. J. Numer Anal. Met. 38 (2014) 518–535.
[56] R. Walker, M. Grotenhuis, A summary of shielding constants for concretes", USAEC Report ANL-6443, Argonne National Laboratory, 1961, in: R.G. Jaeger (Ed.), Engineering Compendium on Radiation Shielding, Springer, Berlin, 1970.